



Synthesis and Characterization of CuO-NiO Nanocomposites for Electrochemical Supercapacitors

Sujit Chatterjee, Apurba Ray, Manas Mandal, Sachindranath Das, and Swapan Kumar Bhattacharya

Submitted: 17 March 2020 / Revised: 19 August 2020 / Accepted: 8 October 2020 / Published online: 6 November 2020

The CuO nanostructures and CuO-NiO nanocomposites of various compositions were successfully synthesized by simple hydrothermal method followed by calcination for investigation of their pseudocapacitive performances. The UV-vis spectroscopy, x-ray diffraction, field emission scanning electron microscopy (FESEM) and high-resolution transmission electron microscopy were used to characterize the as-synthesized electrode materials. Among these different CuO-NiO nanocomposites, CuO(*x*)NiO(100 - *x*), that's with equal mole ratio, CuO(50)NiO(50) exhibits the highest specific capacitance of 35.63 F g⁻¹ at current density of 0.3 A g⁻¹. In addition, it shows excellent cycling stability with capacity retention of 85.7% at 1000th cycle at current density of 10 A g⁻¹. The morphology of CuO(50)NiO(50) nanostructures as determined by FESEM and HRTEM studies, revealed aggregated three-dimensional (3D) hierarchical networks due to aggregation of various parallel 2D thin nanosheets. The supercapacitive activity of the synthesized CuO and CuO-NiO nanomaterials was found to follow the order: CuO(50)NiO(50) > CuO(20)NiO(80) > CuO(100) > CuO(80)NiO(20).

Keywords energy storage, hydrothermal synthesis, nanocomposites, pseudocapacitors

1. Introduction

Of late significant investigations are made to develop sustainable and renewable energy storage devices with high energy, power and reliability to meet the challenges of fossil fuel depletion, global warming, atmospheric pollution, needs in medical and electronic equipments, use of intermittent energy sources, etc. (Ref 1-4). Electrochemical capacitors or supercapacitors have been considered as the most promising energy storage device for sustainable development of human beings than others like lithium-ion batteries, owing to their fast charging-discharging rate, high power density, excellent cyclic stability, safe operation and wide range of working temperature (Ref 5, 6). These may be utilized as primary storer of non-conventional energy like wind, sunlight, etc., and auxiliary (secondary) storer with batteries and fuel cells implanted in cars, mobiles, cordless tools etc., where high power is needed for limited span of time at least occasionally (Ref 7, 8). In general, supercapacitors can be classified into three categories: electrochemical double layer capacitors (EDLCs), pseudocapacitors and hybrid capacitors based on energy storage mechanism (Ref 9, 10). The energy storage mechanism in EDLCs is only non-faradic process. No redox reaction occurs between the electrode and electrolyte. Pseudocapacitors store

charges mainly by reversible faradic redox reactions, where the combination of both faradic and non-faradic processes occur in hybrid supercapacitors (Ref 2, 11-13). The most significant component of electrochemical supercapacitors is active electrode material (Ref 14, 15). Therefore, to design and fabricate low price and environment friendly novel active electrode materials for high-performance supercapacitors is a crucial task. Nowadays, nickel oxide and copper oxide both are emerging electrode materials among various metal oxide pseudocapacitor electrode materials such as RuO₂ and IrO₂ etc., for pseudocapacitor application owing to their low cost, enormous thermal stability, natural abundance and eco-friendliness. Despite nickel oxide and copper oxide both have high theoretical value of capacitance (2573 and 1800 F g⁻¹, respectively), their low electrochemical active surface area, poor electrical conductivity, and poor cycling stability limit their wide application in high-performance supercapacitors (Ref 16-19).

Mixed transition metal oxide (MTMO) is considered promising candidate for wide applications in catalysis, electrocatalysis, sensing, charge storing, etc., (Ref 20-26). MTMO nanocomposites improve the electrochemical performance by enhancing the electrochemical active surface area and charge transfer efficiency. Moreover, when a semiconductor metal oxide nanomaterial of narrow band gap is mixed with that of broad band gap, the composite may exhibit enhanced physiochemical properties compared with each single material. Among the various transition metal oxides, p-type CuO semiconductor oxide has narrow band gap ($E_g = 1.2$ eV), while p-type NiO semiconductor oxide has a wider band gap in the range of 3.6-4.0 eV (Ref 27). Homogeneous precipitation, co-precipitation, sol-gel, thermal decomposition and hydrothermal methods have been successfully employed for the synthesis of mixed metal oxides nanoparticles (Ref 12, 28-30). The physiochemical properties of these nanocomposites largely depend on their size, shape, surface area and porosities. It is reported that the lattices of NiO in NiO-based nanocomposites could produce more electrochemical active sites for supercapacitive activity (Ref 19, 31). For example, Li et al. (Ref 32)

Sujit Chatterjee, Manas Mandal, and Swapan Kumar Bhattacharya, Department of Chemistry, Jadavpur University, Kolkata 700032, India; and Apurba Ray and Sachindranath Das, Department of Instrumentation Science, Jadavpur University, Kolkata 700032, India. Contact e-mail: skbh7@yahoo.co.in.

reported that coral-like mesoporous NiO nanobar could achieve 1085 F g^{-1} at 1 A g^{-1} . Huang et al. (Ref 33) reported that the NiO nanosheets deposited on the nickel foams could exhibit 674.2 F g^{-1} at 1 A g^{-1} . Yan et al. (Ref 34) reported that mesoporous NiO nanoflake arrays could exhibit 400 F g^{-1} at 2 A g^{-1} . Du et al. (Ref 35) reported nano-NiO flower-like microspheres with a maximum specific capacitance of 762 F g^{-1} at 1 A g^{-1} . Min et al. (Ref 36) reported that 2D NiO nanosheet could exhibit high capacitances of 418 F g^{-1} at the current density of 2 A g^{-1} with well cycling stability (still maintained 85% after 2000 cycles). The heterostructured semiconductor oxides involve electron-hole separation. Thus, charges are more stable due to slower rate of recombination. So, mixed oxides are expected to contain more active sites at any moment for electrochemical charge storage and charge transfer (Ref 37-40). Liu et al. (Ref 41) prepared NiO/MnO₂ composite contained 20 wt.% of NiO by sol-gel method exhibited much larger specific capacitance of 453 F g^{-1} at the scanning rate of 10 mV s^{-1} in 6 M KOH electrolyte solution, than that of each pristine component. Zheng et al. (Ref 42) prepared ZnO-Au-NiO composites electrode material with core-shell morphology for supercapacitors which exhibit high areal capacitance of 4.1 F cm^{-2} at a current density of 5 mA cm^{-2} , with excellent cycling stability. Ruan et al. (Ref 43) prepared a three-dimensional porous Ni(OH)₂/Cu₂O/CuO cluster by hydrothermal method exhibited excellent specific capacitance along with excellent cyclic stability. Ray et al. (Ref 44) reported that the three-dimensional mesoporous interlinked tube-like TiO₂-V₂O₅ nanocomposite with molar ratio of 1:2 prepared by wet-chemical method exhibited excellent specific capacitance of 310 F g^{-1} at a scanning rate of 2 mV s^{-1} than individual TiO₂ and V₂O₅ material. Yao et al. (Ref 45) prepared core-shell like NiO@NiCo₂O₄ nanostructures by solvothermal method, which can exhibit excellent specific capacitance along with high cyclic stability.

This idea stimulates us to prepare different CuO(*x*)NiO (100 - *x*) composites for different mole ratio, *x*/(100 - *x*) in order to get improved charge separation and hence synergistic result (Ref 46-49). Herein, we report a facile approach to prepare CuO and various CuO-NiO nanocomposites in absence of any special capping agent via hydrothermal method followed by calcination and tune the surface defects of these electrode materials by controlling the compositions. After assembling asymmetric supercapacitor with CuO(50)NiO(50) electrode material achieves a high energy and power densities of 3.14 Wh kg^{-1} and 507 W kg^{-1} , respectively. In addition, the aggregated Janus-type CuO(50)NiO(50) nanocomposite electrode also exhibits excellent specific capacitance of 35.63 F g^{-1} at current density of 0.3 A g^{-1} and exhibits excellent cycling stability, as 85.7% of the capacitance still retained at 1000th cycle at a high current density of 10 A g^{-1} (Ref 50).

2. Experimental Section

2.1 General Information

The UV-vis spectra were taken by UV-1800 SHIMADZU UV-vis spectrophotometer. X-ray powder diffraction patterns (XRD) of as-synthesized nanoparticles were recorded by a Bruker AXS D8-advance instrument, with Ni-filtered CuK α radiation source ($\lambda = 1.5418 \text{ \AA}$) at 40 kV and 40 mA, employ-

ing a scanning rate of 0.2 degree per second. The morphology of the CuO(50)NiO(50) nanocomposite was obtained using a field emission scanning electron microscope (FESEM, FEI Quanta-250 FEG) operated at 20.00 kV. The transmission electron microscopy (TEM) and high-resolution transmission electron microscopy (HRTEM) images were collected with a Hitachi H-7600 transmission electron microscope.

2.2 Materials

Nickel chloride hexahydrate (NiCl₂·6H₂O), copper sulfate pentahydrate (CuSO₄·5H₂O) and sodium hydroxide (NaOH) were purchased from Merck, India. All chemicals used were of analytical grade and used as received without any further purification. Milli-Q water was used in all experiments.

2.3 Synthesis of CuO, NiO and Various CuO-NiO Composites

In a typical optimized synthesis of CuO(100), 40 mL of 0.5 (M) CuSO₄·5H₂O was added into 40 mL of 1 (M) NaOH solution dropwise under constant stirring at 25 °C for 1 h in a beaker. The obtained blue solution was then transferred into a 100 mL Teflon-lined stainless steel autoclave and then heated at 180 °C for 24 h, and then it was allowed to cool at room temperature. The obtained black precipitate was separated from the solution by centrifugation at 6500 rpm for 5 min (REMI PR-24), washed with Millipore water for three times and finally with ethanol. Then the collected sample was dried in an oven at 80 °C for 24 h. Finally, the as-prepared sample was annealed at 400 °C for 6 h in a hot-air furnace. For synthesis of binary metal oxide composites containing CuO and NiO in the molar ratio of *x*/(100 - *x*), 0.4*x* mL 0.5 M CuSO₄·5H₂O solution was mixed with same volume of 1 M NaOH solution and 0.4(100 - *x*) mL of 0.5 M NiCl₂·6H₂O solution was also mixed with same volume of 1 M NaOH solution separately. The latter solution was added into the former solution with constant stirring for 1 h, at room temperature. Then, the whole mixture was taken in an autoclave for hydrothermal reaction at 180 °C for 24 h, and the rest procedure is maintained as that it was done for the synthesis of CuO(100) (Fig. 1). The general designation of synthesized material was given CuO(*x*)NiO (100 - *x*). By this way three different mixed oxides namely CuO(80)NiO(20), CuO(50)NiO(50) and CuO(20)NiO(80) were prepared. In addition, similarly, NiO(100) was also synthesized by using 0.5 M NiCl₂·6H₂O aqueous solution under same method to investigate the synergistic property of CuO-NiO nanocomposites.

2.4 Electrochemical Studies

The electrochemical performance of the electrode material was greatly influenced by the structure and morphology of the nanocomposites. Electrochemical measurements such as cyclic voltammetry (CV), galvanostatic charge-discharge (GCD), and electrochemical impedance spectroscopy (EIS) were performed with a multichannel electrochemical analyzer (CS313, CorrTest, China) using a three-electrode system immersed in 1 M Na₂SO₄ aqueous solution as an electrolyte at room temperature, taking Ag/AgCl (sat. KCl), a platinum foil (1 cm × 1 cm) and the fabricated nanomaterials deposited on carbon support as reference, counter and working electrodes, respectively. To prepare the working electrode, a Teflon-coated graphite rod (4 mm diameter) was used as the current collector. The working electrode was prepared by mixing the as-prepared active

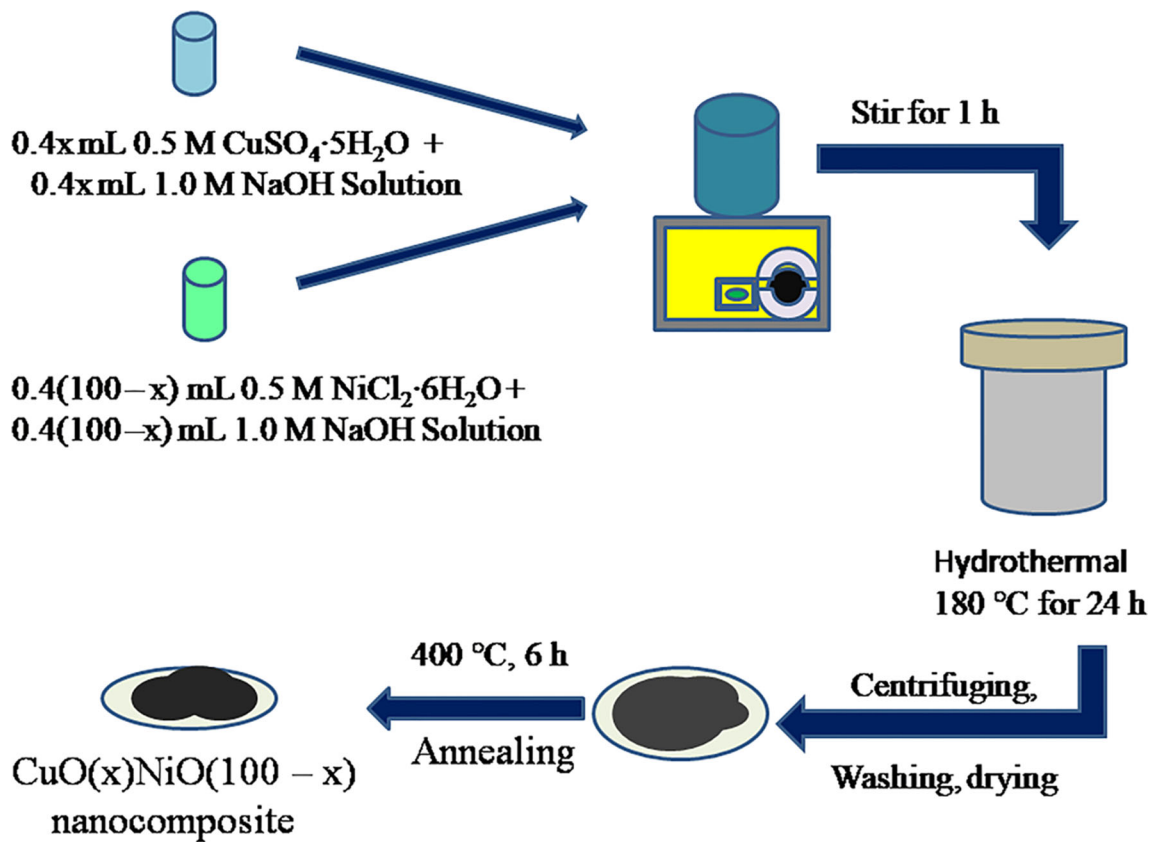


Fig. 1 Schematic representation of the synthesis of $\text{CuO}(x)\text{NiO}(100 - x)$ active electrode materials

electrode material (80 wt.%), activated carbon (15 wt.%) and polyvinylidene difluoride (PVDF, 5 wt.%) in 200 μL of N-methyl pyrrolidine (NMP) solution and sonicated it for 30 min to form a gel. Next, the gel was drop-casted on the one flat end of the Teflon-covered graphite rod, and finally the electrode was dried at 60 $^{\circ}\text{C}$ for 6 h, and the deposited mass of the as-synthesized active electrode material was approximately 1.0 mg. Electrochemical impedance spectroscopy study was performed in the frequency range of 0.01 Hz to 100 kHz with an AC perturbation amplitude of 10 mV. EC-Lab software was used to fit the EIS data. The accurate specific capacitance (C_{sp}) in F g^{-1} for all CuO and CuO-NiO nanocomposite active electrode materials in three-electrode system has been calculated from the galvanostatic discharge curves based on Eq 1.

$$C_{\text{sp}} = \frac{I \times \Delta t}{m \times \Delta V} \quad (\text{Eq 1})$$

where m is the mass of the active electrode material in working electrode (g), I/m is the current density (A g^{-1}), Δt is the discharge time (s), and ΔV is the applied potential (V) window.

The energy density (E_{cell}) (Wh kg^{-1}) and power density (P_{cell}) (W kg^{-1}) of the fabricated active electrode materials were calculated using Eq 2 and 3, respectively,

$$E_{\text{cell}} = \frac{1}{2 \times 3.6} \times C_{\text{sp}} \times \Delta V^2 \quad (\text{Eq 2})$$

$$P_{\text{cell}} = \frac{3600 \times E_{\text{cell}}}{\Delta t} \quad (\text{Eq 3})$$

where C_{sp} is the specific capacitance (F g^{-1}), Δt is the discharge time (s), and ΔV is the applied potential (V) window.

3. Results and Discussion

The UV-vis absorption spectra of the synthesized CuO nanoparticles and CuO-NiO nanocomposites are presented in Fig. 2. It is evident that the $\text{CuO}(50)\text{NiO}(50)$ nanocomposite shows sharp absorption peak at 323 nm, while others synthesized nanomaterials exhibit weak absorption peaks. This clearly indicates that the decrease in the value of band gap of $\text{CuO}(50)\text{NiO}(50)$ nanocomposite may be attributed to easy charge separation, improvement in the crystalline quality of the 3D nano network as well as to the decrease in grain size (Ref 51). The peak positions are shifted toward lower wavelength as mol.% of NiO is increased in $\text{CuO}(x)\text{NiO}(100 - x)$ mixed materials, as evidenced in Fig. 2(a) and (b). Figure 2(b) is the expanded picture of a part of Fig. 2(a). The absorption peaks of $\text{CuO}(100)$, $\text{CuO}(80)\text{NiO}(20)$ and $\text{CuO}(20)\text{NiO}(80)$ are 389, 348 and 264 nm, respectively.

The crystal structure and phase purity of the fabricated nanomaterials were determined by x-ray diffraction (XRD). The profiles were presented in Fig. 3. Figure 3(a) shows the x-ray diffraction patterns of $\text{CuO}(100)$ nanoparticles, $\text{CuO}(80)\text{NiO}(20)$ and $\text{CuO}(20)\text{NiO}(80)$ nanocomposites. The x-ray diffraction patterns of $\text{CuO}(50)\text{NiO}(50)$ nanocomposite and $\text{NiO}(100)$ are shown in Fig. 3(b) and (c), respectively. The diffraction peaks of $\text{CuO}(100)$ at 32.55° , 35.56° , 38.80° ,

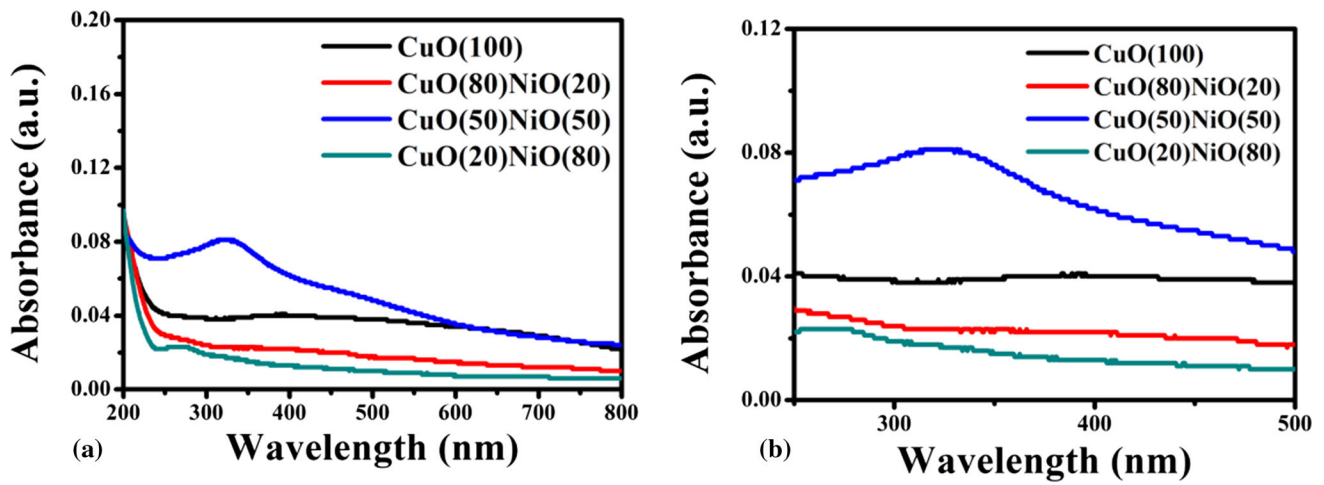


Fig. 2 (a) The UV-vis. spectra of diluted aqueous solutions of same mass of CuO(100), CuO(80)NiO(20), CuO(50)NiO(50) and CuO(20)NiO(80) nanomaterials (b) parts of the same spectra in expanded form

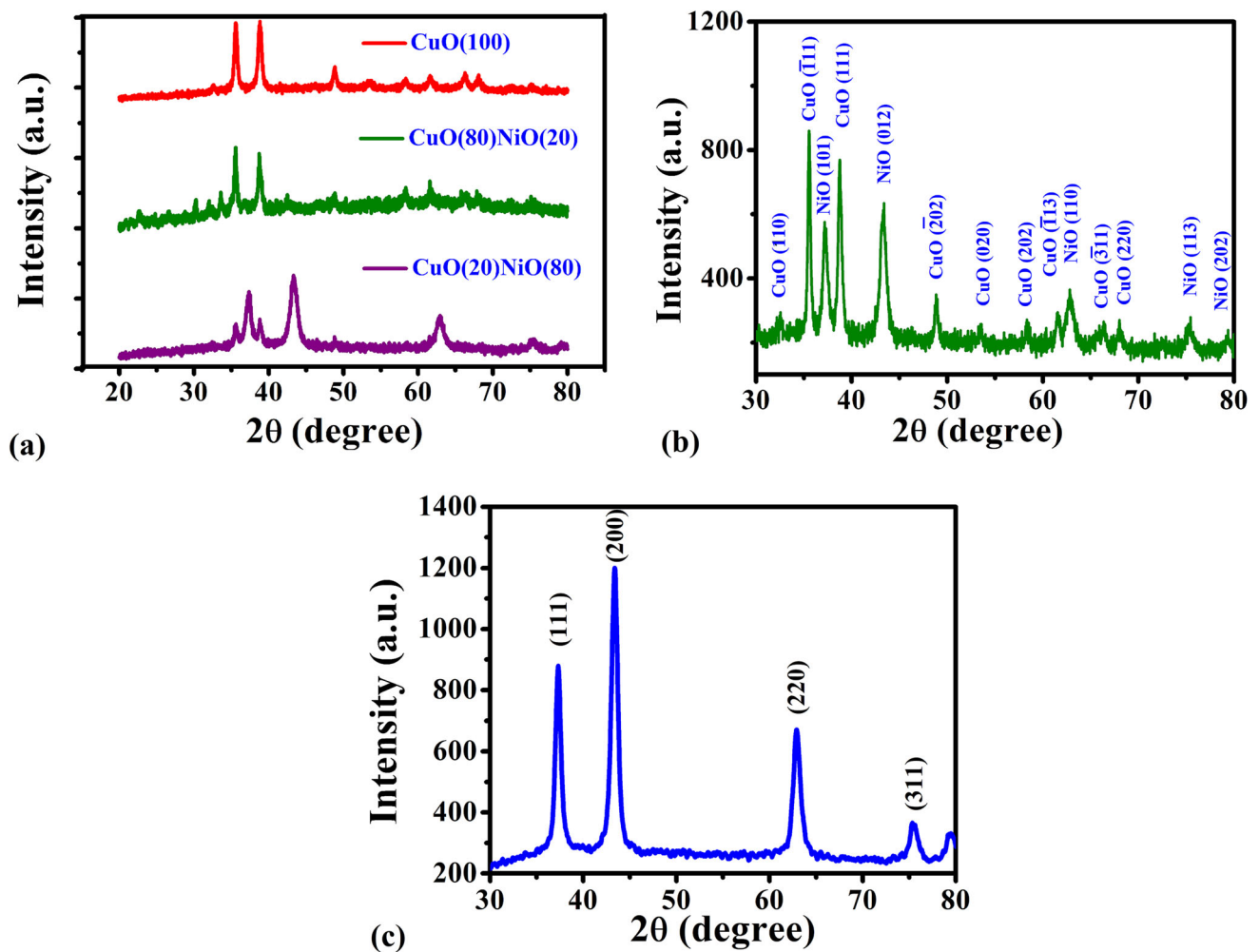


Fig. 3 X-ray diffraction patterns of the (a) CuO(100), CuO(80)NiO(20), CuO(20)NiO(80), (b) CuO(50)NiO(50), and (c) NiO(100) nanomaterials, respectively

48.79°, 53.6°, 58.37°, 66.29°, 68.17°, 72.5° and 75.3° correspond to the (110), (111), (111), (202), (020), (202), (311), (220), (311) and (2 22) planes of end-centered-monoclinic CuO

(JCPDS card No. 80-1268), while the diffraction peak at 2θ value of 61.4° correspond to the (220) plane of cubic Cu₂O (JCPDS card No. 78-2076), respectively. The diffraction peaks

of CuO(80)NiO(20), CuO(20)NiO(80), and CuO(50)NiO(50) nanocomposites at 32.55°, 35.56°, 38.80°, 48.79°, 53.6°, 58.37°, 66.29°, 68.17°, 72.5°, 75.3° correspond to the (110), ($\bar{1}11$), (111), ($\bar{2}02$), (020), (202), ($\bar{3}11$), (220), (311), ($\bar{2}22$) planes of end-centered-monoclinic CuO [JCPDS card No. 80-1268], while the peaks at 37.2°, 43.29°, 62.8°, 75.4°, and 79.4° are associated with (111), (200), (220), (311), and (222) planes of face-centered-cubic NiO [JCPDS card No. 78-0429], respectively. For the CuO(80)NiO(20) sample, while the rest of the diffraction peaks at 2θ values of 29.6° and 61.4° are due to the (110) and (220) planes of cubic Cu₂O [JCPDS card No. 78-2076], respectively (Ref 52). It is to be noted that no characteristic Cu₂O peaks were found in CuO(20)NiO(80), and CuO(50)NiO(50) nanocomposites. The average grain sizes of CuO and NiO nanoparticles of CuO(50)NiO(50) nanocomposite have been determined from the most intense peak of XRD pattern using Debye-Scherrer formula, are 18, and 6 nm for NiO and CuO nanoparticles, respectively (Ref 6). Similarly the average grain size of CuO(80)NiO(20) and CuO(20)NiO(80) nanocomposites can be calculated from the most intense peaks of the corresponding profile as 36 and 17 nm for CuO and 34 and 9 nm for NiO, respectively. Moreover, the average grain diameter of CuO(100) nanomaterial is 17 nm.

The structure and morphology of the as-synthesized CuO(50)NiO(50) nanocomposite was investigated by field emission scanning electron microscopy and high-resolution transmission electron microscopy. Figure 4 shows the FESEM image of as-prepared CuO(50)NiO(50) nanocomposite. FESEM image clearly reveals that the aggregated hierarchical three-dimensional (3D) nanostructures are consisted of parallel self-assembled nanosheets, which may provide high electrochemical active specific surface area as well as higher degree of diffusion of the ions of electrolyte to the CuO(50)NiO(50) electrode and thus result in higher capacitance. The TEM, HRTEM images, SAED pattern, and the particles distribution curves of the as-synthesized CuO(50)NiO(50) nanocomposite are shown in Fig. 5. TEM image (Fig. 5a) shows aggregated but two definitely separated black and gray parts which might

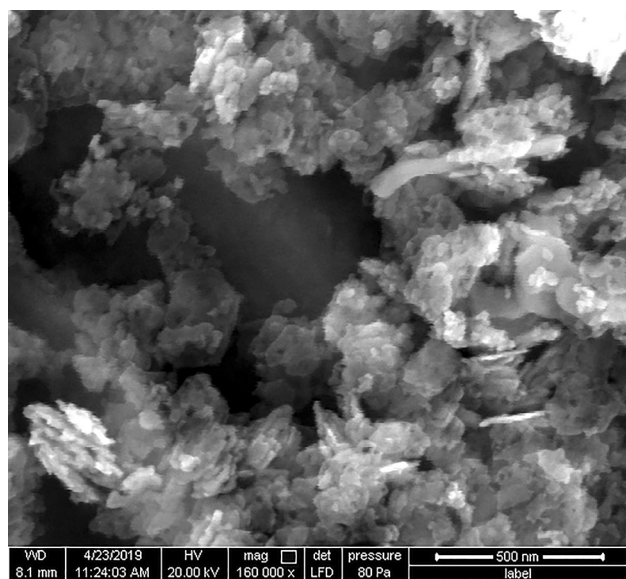


Fig. 4 FESEM image of the CuO(50)NiO(50) nanocomposite

be called Janus-type nanostructure of CuO(50)NiO(50) nanocomposite. Figure 5(b) shows the HRTEM image of as-synthesized CuO(50)NiO(50) nanocomposite, clearly reveal the stacked aggregated nanostructure, which is consistent with the FESEM result. In addition, HRTEM exhibits the lattice-fringes with spacing between the adjacent lattice planes of 0.212 and 0.241 nm, corresponding to the (200) plane of fcc CuO [JCPDS card No. 78-0428] and (111) plane of fcc NiO [JCPDS card No. 78-0429] of as-synthesized CuO(50)NiO(50) nanocomposite as shown in Fig. 5(b). The SAED pattern of CuO(50)NiO(50) nanocomposite is shown in Fig. 5(c), which confirms the presence of (111), (220), and (311) planes corresponding to the lattice fringes with the spacing of 0.241, 0.147, and 0.126 nm of cubic crystalline NiO and (200) plane corresponding to the lattice fringes with the spacing of 0.212 nm of cubic CuO, respectively. Additionally, the typical TEM image (the inset of Fig. 5a) and the HRTEM image (Fig. 5d) show the Janus-type asymmetric nanostructures of CuO(50)NiO(50) nanocomposite. Figure 5(e) and (f) depict the particle size distribution profiles of CuO and NiO of CuO(50)NiO(50) nanocomposite. The average diameter of CuO and NiO nanoparticles are found 4.0 nm and 23.1 nm, respectively.

Figure 6 shows the cyclic voltammograms of CuO(100) and CuO(x)NiO(100 - x)-based electrodes immersed in 1 M Na₂SO₄, obtained by application of various scan rates ranging between 2 to 100 mV s⁻¹ within the potential window of 0 to 1.0 V, at room temperature. The shape of the CV curves of all the four electrodes clearly reveals the typical pseudocapacitive behaviors of the electrodes. Figure 6 clearly reveals that the area of the CV curves is increased with increasing the scan rate from 2 to 100 mV s⁻¹. Moreover, the cyclic voltammograms of CuO(80)NiO(20) and CuO(100) exhibit a prominent anodic peak at potential around 0.23 V at the scan rates of 2 and 5 mV s⁻¹ as shown in Fig. 6(b) and (e), respectively, due to the following faradic reaction (Ref 18, 52):

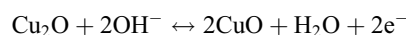


Figure 7(a) reveals that the specific capacitance is decreased with increasing the potential speed. On increasing the potential speed, the electrolyte ions become unable to move at par and thus unable to contact with the inner surface of the electrode fully, causing a decrease in specific capacitance. To investigate the charge storage mechanism of CuO(100) and CuO-NiO nanocomposites having different compositions the relationship between scan rates (v) and anodic peak currents (I_p) are analyzed with help of the following equation (Eq 4):

$$I_p = a \times v^b \quad (\text{Eq 4})$$

where 'a' and 'b' are adjustable parameters. For $b = 1$, the charge storage mechanism is mainly surface-controlled, while $b = 0.5$ represents that the said mechanism is diffusion-controlled process. The obtained b values of CuO(100) and CuO-NiO nanostructures (Fig. 7b) are 0.61, 0.60, 0.82 and 0.61, respectively, for CuO(100), CuO(80)NiO(20), CuO(50)-NiO(50), and CuO(20)NiO(80) nanomaterials, respectively, suggesting that the total specific capacitance is due to both surface-controlled and diffusion-controlled processes. Surface-controlled capacitance (C_{in}) and diffusion-controlled capacitance (C_{out}) are expressed by the Trasatti relation (Eq 5).

$$C_{\text{Total}}(\text{F g}^{-1}) = C_{in} + C_{out} \quad (\text{Eq 5})$$

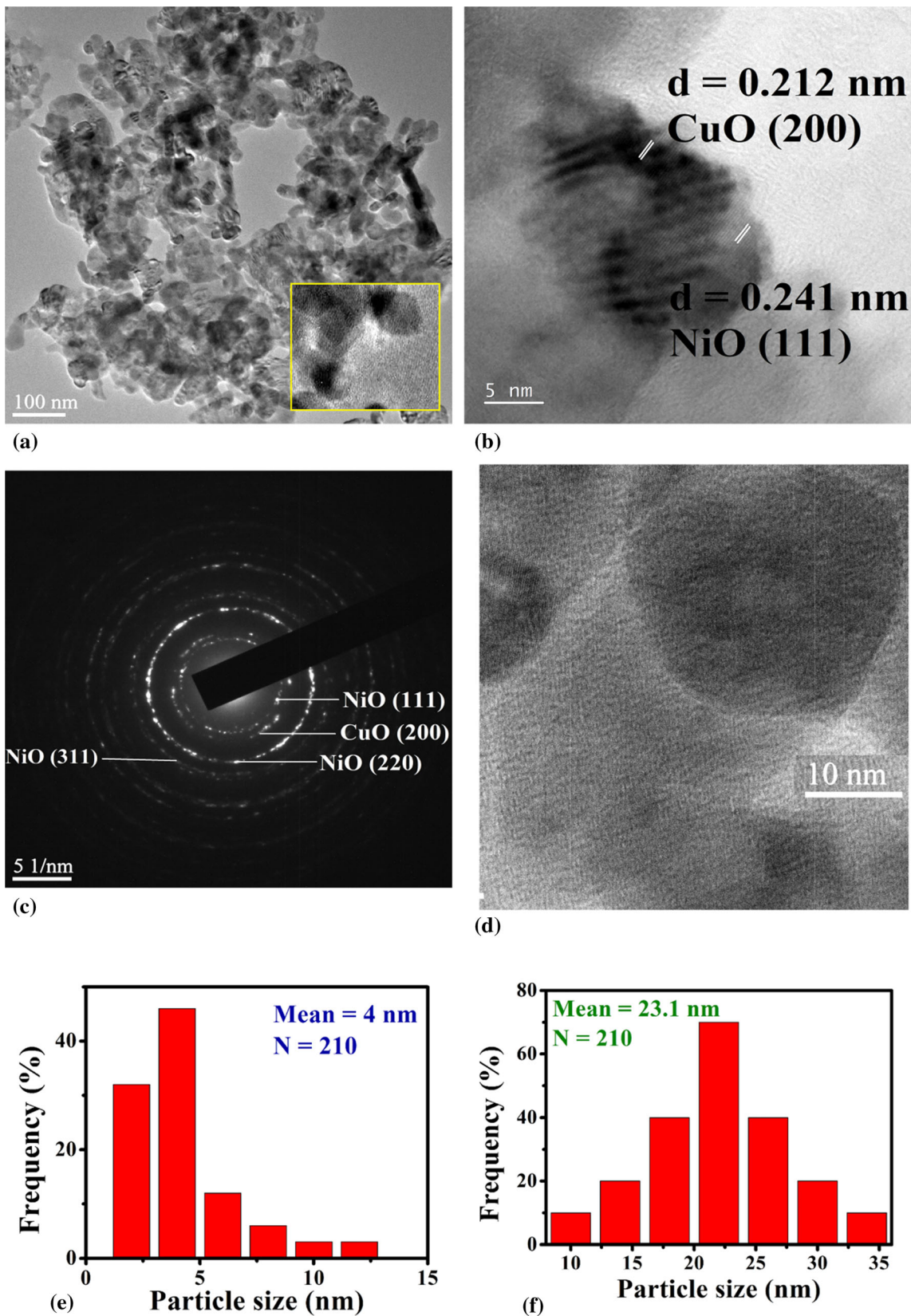


Fig. 5 (a) TEM image showing Janus-type structure at the inset (b) HRTEM image, (c) SAED pattern and (d) HRTEM image showing, Janus-type structure of CuO(50)NiO(50) nanocomposite, with particles size distribution curve of (e) CuO and (f) NiO nanoparticles from TEM images

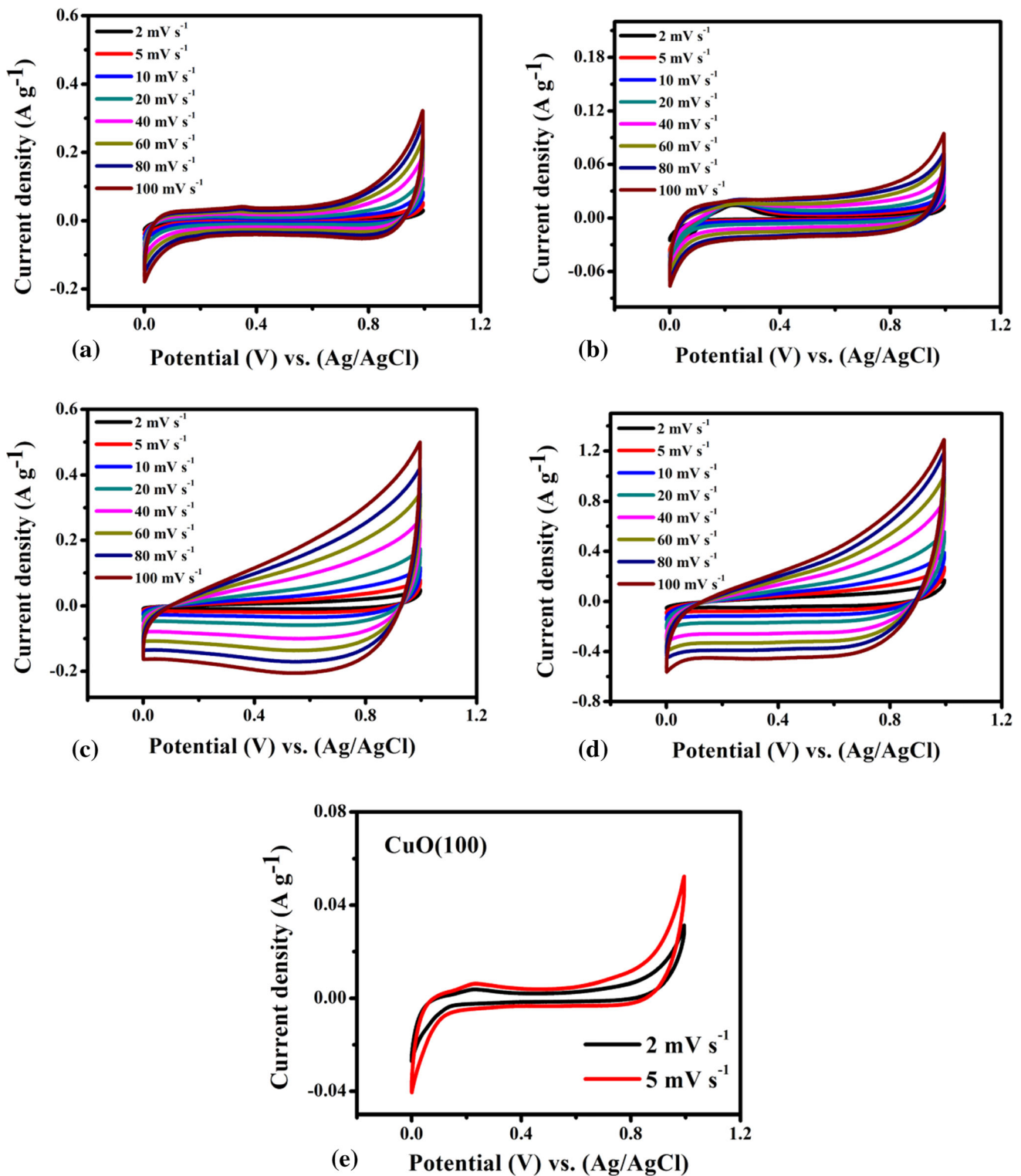


Fig. 6 CV curves of (a) CuO(100), (b) CuO(80)NiO(20), (c) CuO(50)NiO(50) and (d) CuO(20)NiO(80) nanomaterials at different scan rates ranging from 2 to 100 mV s⁻¹ and (e) cyclic voltammogram of the CuO(100) at the scan rates of 2 and 5 mV s⁻¹

The maximum possible capacity, C_{Total} and the capacity due to outer surface, C_{out} can be determined by extrapolating the specific capacitance (C_{sp}) versus $(v)^{1/2}$ (Fig. 7c) and specific capacitance (C_{sp}) versus $(v)^{-1/2}$ (Fig. 7d), respectively. C_{Total} (F

g⁻¹) for CuO(100), CuO(80)NiO(20), CuO(50)NiO(50) and CuO(20)NiO(80) are found 2.74, 2.8, 6.03 and 26.16, respectively. Moreover, C_{out} (F g⁻¹) for these electrodes is 0.33, 0.30, 1.23 and 1.20, respectively, indicating that the contribution of

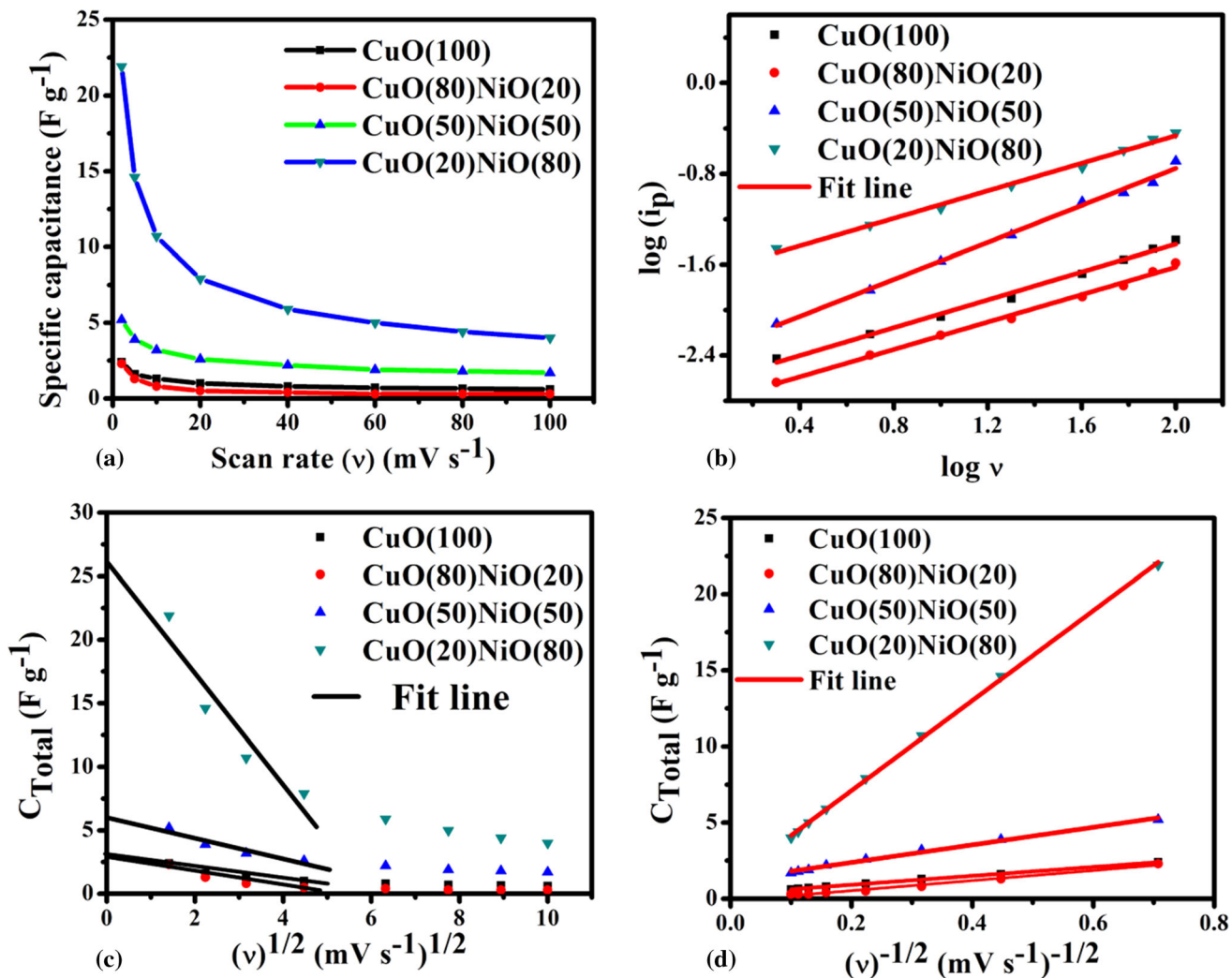


Fig. 7 (a) Specific capacitance variation with different scan rates, (b) $\log(i_p)$ vs. $\log(v)$ plots, (c) C_{Total} vs. $v^{1/2}$ and (d) C_{Total} vs. $v^{-1/2}$ of CuO(100), CuO(80)NiO(20), CuO(50)NiO(50) and CuO(20)NiO(80)-based electrodes

capacity by outer surface is almost same for the last two electrodes. Overall the electrodes which contain sufficient amount say 50–80 mol.% of NiO seem to be better than others.

The galvanostatic charge/discharge (GCD) cycles at different current densities for CuO(100), CuO(80)NiO(20), CuO(50)NiO(50) and CuO(20)NiO(80) are shown in Fig. 8. The specific capacitance for all the electrode materials computed from the GCD plots (Fig. 9a) shows that the maximum C_{sp} values obtained are 3.95, 0.6, 22.6 and 6.37 F g⁻¹ at current density of 1 A g⁻¹ for CuO(100), CuO(80)NiO(20), CuO(50)NiO(50) and CuO(20)NiO(80), respectively. GCD profiles (Fig. 8) reveal that the capacity of the electrodes follows the order CuO(50)NiO(50) > CuO(20)NiO(80) > CuO(100) > CuO(80)NiO(20). Figure 9(b) displays that the specific capacitance decreased with increasing charge–discharge current density. The specific capacitance values are 35.6, 29.6, 25.5, 22.6, 22.56 and 14.4 F g⁻¹ at current densities of 0.3, 0.5, 0.7,

0.9, 1.0 and 3.0 A g⁻¹ for CuO(50)NiO(50) nanocomposite electrode. In order to examine synergistic effect of CuO(50)NiO(50) nanocomposite, we have synthesized NiO(100) active electrode materials by the same procedure as stated above like CuO(100), and GCD experiments was performed for these three electrodes at current density of 0.3 A g⁻¹ within the potential window of 0 to 1.0 V. Figure 10 shows the galvanostatic charge/discharge curves of CuO(100), NiO(100), and CuO(50)NiO(50) electrodes at a mass normalized current of 0.3 A g⁻¹. The calculated specific capacitances using Eq 1, are 5, 25 and 36 F g⁻¹, respectively, indicating CuO(50)NiO(50) nanocomposite exhibits excellent supercapacitive performance than CuO(100) and NiO(100) due to synergistic effects between nickel oxide and copper oxide (Ref 6, 53).

Figure 9(c) depicts the EIS plot of as-prepared electrodes in the frequency range of 0.01 Hz to 100 kHz in 1 M Na₂SO₄ at a

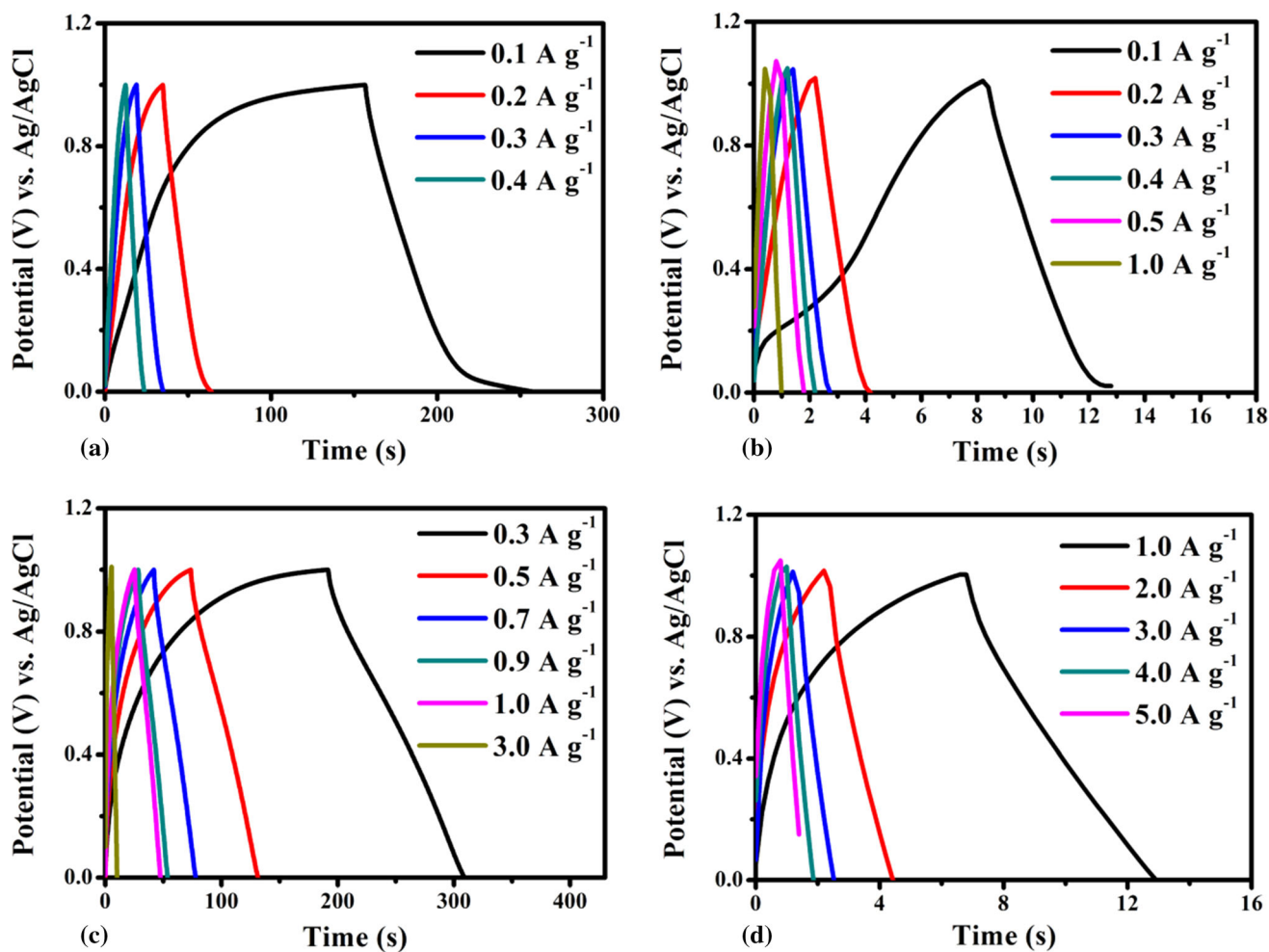


Fig. 8 GCD curves of (a) CuO(100), (b) CuO(80)NiO(20), (c) CuO(50)NiO(50) and (d) CuO(20)NiO(80) electrodes at different current densities

fixed dc potential of 0.5 V. The inset of Fig. 9(c) presents the fitting circuit diagram. The EIS plots for as-prepared electrode show small semicircles at high frequency region and the sloped lines in the low-frequency region, indicating the charge-transfer resistance (R_{ct}) and Warburg impedance (W_0), respectively. Moreover, in the fitting circuit, R_s , C_{dl} and C_p are the solution resistance, double layer capacitance and the pseudocapacitance, respectively. The different electrochemical parameters obtained from the EIS study are presented in Table 1. The smaller the charge-transfer resistance (R_{ct}), solution resistance (R_s) and the larger pseudocapacitance (C_p) value of CuO(50)NiO(50) nanocomposite compared to the other materials due to synergistic effect suggesting faster electrochemical reaction on the electrode. The lower value of Warburg impedance (W_0) of CuO(50)NiO(50) nanocomposite also signifies the better diffusion of electrolyte ions with the stacked 2D nanosheets.

Figure 9(e) shows that the coulombic efficiency of CuO(50)NiO(50) electrode, at a current density of 10 A g^{-1} . The reduction of coulombic efficiency of CuO(50)NiO(50) electrode in the beginning has been observed due to the activation effect of the active electrode materials. As the number of repeated charge–discharge (CD) cycles increases, the adsorption-desorption of electrolyte ions is increased into the stacked nanosheets of active electrode materials and more electrochemically active redox sites of electrodes get in direct contact with the electrolyte, leading to increase of coulombic efficiency. Up to a certain number of charge–discharge cycles, the maximum activation process of the stacked nanosheets of CuO(50)NiO(50) nanocomposite occur, and after that it gets saturated. During the CD cycles the volume expansion of the electrode materials occur, which improves the infiltration of the electrolyte ions within the stacked nanosheets of the electrodes

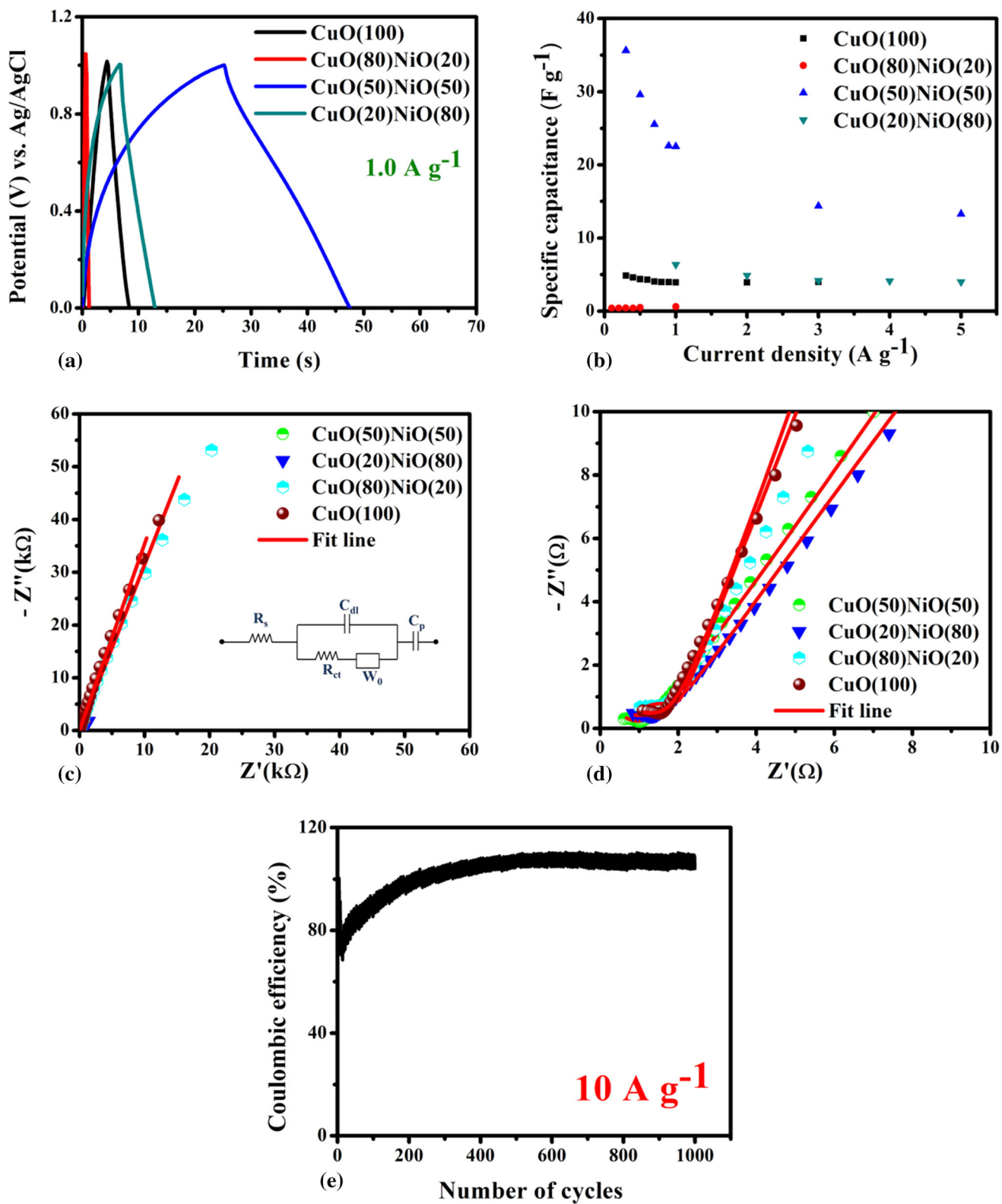


Fig. 9 (a) GCD curves at a constant current density of 1 A g^{-1} (b) specific capacitance at different current densities of CuO(100), CuO(80)NiO(20), CuO(50)NiO(50) and CuO(20)NiO(80) electrodes, (c) Nyquist plots with equivalent circuit diagram at the inset (d) Nyquist plots at high frequency region of CuO(50)NiO(50), CuO(20)NiO(80), CuO(80)NiO(20), CuO(100)-based electrodes and (e) coulombic efficiency vs. cycle number for CuO(50)NiO(50)-based electrode at a current density of 10 A g^{-1}

(Ref 54). The specific capacitances of CuO(50)NiO(50) nanocomposite are found to be 14, 12 and 12 F g⁻¹ for first, 500, and 1000 cycles, respectively, the specific capacitance could keep 85.7% capacity retention at 1000 cycle, demonstrating its good cycling stability (Fig. 11). This CuO(50)-NiO(50) nanocomposite electrode offers the highest energy density (E_{cell}) and power density (P_{cell}) compared to other electrodes as shown in Table 2.

4. Conclusions

In summary, different CuO-NiO mixed oxides containing NiO in the range of 20–80 mol.% are synthesized for efficient supercapacitor application. The CuO(50)NiO(50) nanocomposite is found to be the best one for improved and synergistic specific capacity, energy density, power density, etc., because of

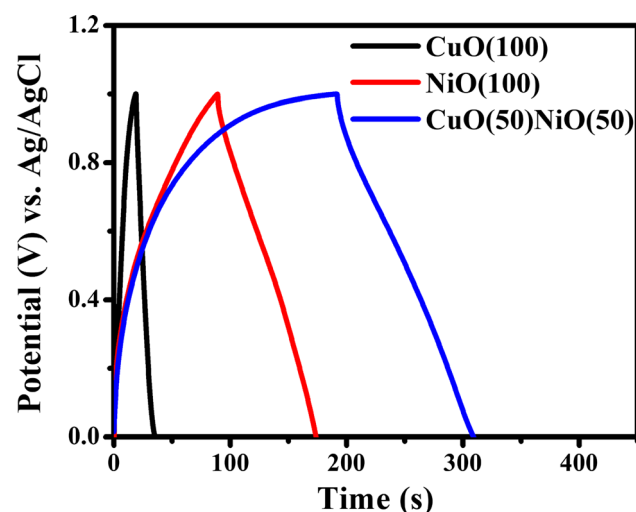


Fig. 10 Galvanostatic charge/discharge profiles of CuO(100), NiO(100) and CuO(50)NiO(50) nanocomposite-based electrodes at a current density of 0.3 A g⁻¹

its optimum composition and unique Janus-type nanostructure with stacked 2D nanosheet morphology. The particle dimension can be reduced and porosity may be increased by suitable modification of the synthesis protocol and better fabrication for more efficient devices.

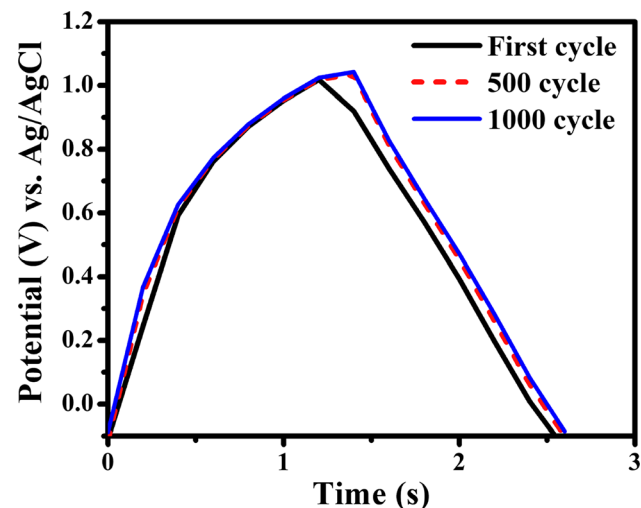


Fig. 11 Galvanostatic charge/discharge profiles of CuO(50)NiO(50) at the 1st, 500th and 1000th cycles at a current density of 10 A g⁻¹

Table 2 Values of energy densities (E_{cell}) and power densities (P_{cell}) of different electrodes at current density of 1 A g⁻¹

Sl. no.	Nanomaterials	E_{cell} , Wh kg ⁻¹	P_{cell} , W kg ⁻¹
1	CuO(100)	0.55	501.3
2	CuO(80)NiO(20)	0.08	500
3	CuO(50)NiO(50)	3.14	507
4	CuO(20)NiO(80)	0.89	503

Table 1 Electrochemical parameters of CuO(100), and CuO-NiO nanocomposites estimated through EIS study

Samples	R_s , Ω	R_{ct} , Ω	C_{dl} , mF cm ⁻²	C_p , mF cm ⁻²	W_0 , Ω s ^{-1/2}	Goodness of fitting (χ^2)
CuO(50)NiO(50)	0.26	0.86	2.565	7.318	6.76	0.040
CuO(20)NiO(80)	0.33	1.04	0.364	1.519	16.82	0.054
CuO(80)NiO(20)	0.35	1.95	0.658	0.185	109.70	0.082
CuO(100)	0.41	1.53	0.873	0.263	592.15	0.052

Acknowledgments

Authors acknowledge to Department of Chemistry and Department of Instrumentation Science of Jadavpur University for instrumental helps and financial supports.

Conflict of interest

The authors declare that they have no conflict of interest.

References

1. F. Wang, X. Wu, X. Yuan, Z. Liu, Y. Zhang, L. Fu, Y. Zhu, Q. Zhou, Y. Wu, and W. Huang, Latest Advances in Supercapacitors: from New Electrode Materials to Novel Device Designs, *Chem. Soc. Rev.*, 2017, **46**, p 6816–6854
2. A. Ray, A. Roy, M. Ghosh, J.A. Ramos-Ramón, S. Saha, U. Pal, S.K. Bhattacharya, and S. Das, Study on Charge Storage Mechanism in Working Electrodes Fabricated by Sol-Gel Derived Spinel NiMn₂O₄ Nanoparticles for Supercapacitor Application, *Appl. Surf. Sci.*, 2019, **463**, p 513–525
3. J. Hassoun, K.S. Lee, Y.K. Sun, and B. Scrosati, An Advanced Lithium Ion Battery Based on High Performance Electrode Materials, *J. Am. Chem. Soc.*, 2011, **133**(9), p 3139–3143
4. Z. Yang, Z. Li, P. Li, C. Gao, and H. Zhang, NiO/Ni Nanocomposites Embedded in 3D Porous Carbon with High Performance for Lithium-Ion Storage, *J. Mater. Sci.*, 2020, **55**, p 1659–1672
5. K. Zhang, Q. Wang, A. Thota, W. Zhang, J. Chen, Y. Wang, X. Wu, and S. Wang, Flexible 3D Hierarchical Porous NiCo₂O₄/CC Electrode Decorated by Nitrogen-Doped Carbon from Polyaniline Carbonization for High-Performance Supercapacitors, *J. Mater. Sci.*, 2020, **55**, p 5982–5993
6. A. Ray, A. Roy, S. Saha, M. Ghosh, S. Roy Chowdhury, T. Maiyalagan, S.K. Bhattacharya, and S. Das, Electrochemical Energy Storage Properties of Ni-Mn-Oxide Electrodes for Advance Asymmetric Supercapacitor Application, *Langmuir*, 2019, **35**, p 8257–8267
7. D.P. Dubal, O. Ayyad, V. Ruiz, and P. Gómez-Romero, Hybrid Energy Storage: The Merging of Battery and Supercapacitor Chemistries, *Chem. Soc. Rev.*, 2015, **44**, p 1777–1790
8. J. Chen, N. Chen, X. Feng, and W. Hou, Preparation of Shape-Controlled Graphene/Co₃O₄ Composites for Supercapacitors, *J. Mater. Eng. Perform.*, 2016, **25**(9), p 3845–3851
9. S. Najib and E. Erdem, Current Progress Achieved in Novel Materials for Supercapacitor Electrodes: Mini Review, *Nanoscale Adv.*, 2019, **1**, p 2817–2827
10. Y. Shao, M.F. El-Kady, J. Sun, Y. Li, Q. Zhang, M. Zhu, H. Wang, B. Dunn, and R.B. Kaner, Design and Mechanisms of Asymmetric Supercapacitors, *Chem. Rev.*, 2018, **118**, p 9233–9280
11. S.H. Kang, B.N. Kim, and I.G. Kim, Facile Synthesis of Porous Carbon Via Self-Activation of Potassium Acetate for High-Performance Supercapacitor Electrodes with Excellent Cyclic Stability, *Energy Technol.*, 2019, **7**, p 1801090
12. H. Pal, S. Bhubna, P. Kumar, R. Mahapatra, and S. Chatterjee, Synthesis of Flexible Graphene/Polymer Composites for Supercapacitor Applications, *J. Mater. Eng. Perform.*, 2018, **27**, p 2668–2672
13. A. Roy, A. Ray, S. Saha, M. Ghosh, T. Das, B. Satpati, M. Nandi, and S. Das, NiO-CNT Composite for High Performance Supercapacitor Electrode and Oxygen Evolution Reaction, *Electrochim. Acta*, 2018, **283**, p 327–337
14. G. Wang, L. Zhang, and J. Zhang, A Review of Electrode Materials for Electrochemical Supercapacitors, *Chem. Soc. Rev.*, 2012, **41**, p 797–828
15. D. Majumdar, M. Mandal, and S.K. Bhattacharya, V₂O₅ and Its Carbon-Based Nanocomposites for Supercapacitor Applications, *ChemElectroChem*, 2019, **6**, p 1623–1648
16. R.S. Kate, S.A. Khalate, and R.J. Deokate, Overview of Nanostructured Metal Oxides and Pure Nickel Oxide (NiO) Electrodes for Supercapacitors: A Review, *J. Alloys Compd.*, 2018, **734**, p 89–111
17. A.K. Singh, D. Sarkar, G.G. Khan, and K. Mandal, Hydrogenated NiO Nanoblock Architecture for High Performance Pseudocapacitor, *ACS Appl. Mater. Interfaces*, 2014, **6**, p 4684–4692
18. J. Ye, Z. Li, Z. Dai, Z. Zhang, M. Guo, and X. Wang, Facile Synthesis of Hierarchical CuO Nanoflower for Supercapacitor Electrodes, *J. Electron. Mater.*, 2016, **45**(8), p 4237–4245
19. X. Ren, C. Guo, L. Xu, T. Li, L. Hou, and Y. Wei, Facile Synthesis of Hierarchical Mesoporous Honeycomb-like NiO for Aqueous Asymmetric Supercapacitors, *ACS Appl. Mater. Interfaces*, 2015, **7**, p 19930–19940
20. S. Chandra Sekhar, G. Nagaraju, and J.S. Yu, High-Performance Pouch-Type Hybrid Supercapacitor Based on Hierarchical NiO-Co₃O₄-NiO Composite Nanoarchitectures as an Advanced Electrode Material, *Nano Energy*, 2018, **48**, p 81–92
21. L.M. Toscani, M.G. Zimicz, T.S. Martins, D.G. Lamas, and S.A. Larrondo, In Situ X-ray Absorption Spectroscopy Study of CuO-NiO/CeO₂-ZrO₂ Oxides: Redox Characterization and Its Effect in Catalytic Performance for Partial Oxidation of Methane, *RSC Adv.*, 2018, **8**, p 12190–12203
22. E.F. AboZeid, A.M. Nassar, M.A. Hussein, M.M. Alam, A.M. Asiri, H.H. Hegazy, and M.M. Rahman, Mixed Oxides CuO-NiO Fabricated for Selective Detection of 2-Aminophenol by Electrochemical Approach, *J. Mater. Res. Technol.*, 2020, **9**(2), p 1457–1467
23. K. Ghanbari and Z. Babaei, Fabrication and Characterization of Non-enzymatic Glucose Sensor Based on Ternary NiO/CuO/Polyaniline Nanocomposite, *Anal. Biochem.*, 2016, **498**, p 37–46
24. X. Zhao, X. Liu, F. Li, and M. Huang, MnO₂@NiO Nanosheets@Nanowires Hierarchical Structures with Enhanced Supercapacitive Properties, *J. Mater. Sci.*, 2020, **55**(6), p 2482–2491
25. M.P. Chavhan, S.R. Sethi, and S. Ganguly, Mixed Metal Oxides in Synergy at Nanoscale: Electrospray Induced Porosity of In Situ Grown Film Electrode for Use in Electrochemical Capacitor, *Electrochim. Acta*, 2020, **347**, p 136277
26. A.Y. Faid and H. Ismail, Ternary Mixed Nickel Cobalt Iron Oxide Nanorods as a High Performance Asymmetric Supercapacitor Electrode, *Mater. Today Energy*, 2019, **13**, p 285–292
27. L. Arun, C. Karthikeyan, D. Philip, and C. Unni, Optical, Magnetic, Electrical, and Chemo-catalytic Properties of Biosynthesized CuO/NiO Nanocomposites, *J. Phys. Chem. Solids*, 2020, **136**, p 109155
28. D. Majumdar and S.K. Bhattacharya, Sonochemically Synthesized Hydroxy-Functionalized Graphene-MnO₂ Nanocomposite for Supercapacitor Applications, *J. Appl. Electrochem.*, 2017, **47**, p 789–801
29. D. Majumdar, N. Baugh, and S.K. Bhattacharya, Ultrasound Assisted Formation of Reduced Graphene Oxide-Copper (II) Oxide Nanocomposite for Energy Storage Applications, *Colloid. Surf. A physiochem. Eng. Asp.*, 2017, **512**, p 158–170
30. X. Zhang, W. Shi, J. Zhu, W. Zhao, J. Ma, S. Mhaisalkar, T.-L. Maria, Y. Yang, H. Zhang, H.-H. Hng, and Q. Yan, Synthesis of Porous NiO Nanocrystals with Controllable Surface Area and Their Application as Supercapacitor Electrodes, *Nano Res.*, 2010, **3**(9), p 643–652
31. Y. Jiao, W. Hong, P. Li, L. Wang, and G. Chen, Metal-Organic Framework Derived Ni/NiO Micro-particles with Subtle Lattice Distortions for High-Performance Electrocatalyst and Supercapacitor, *Appl. Catal. B*, 2019, **244**, p 732–739
32. J. Li, F. Luo, Q. Zhao, Z. Li, H. Yuan, and D. Xiao, Coprecipitation Fabrication and Electrochemical Performances of Coral-like Mesoporous NiO Nanobars, *J. Mater. Chem. A*, 2014, **2**, p 4690–4697
33. M. Huang, F. Li, J.Y. Ji, Y.X. Zhang, X.L. Zhao, and X. Gao, Facile Synthesis of Single-crystalline NiO Nanosheet Arrays on Ni Foam for High-performance Supercapacitors, *CrystEngComm*, 2014, **16**, p 2878–2884
34. X. Yan, X. Tong, J. Wang, C. Gong, M. Zhang, and L. Liang, Synthesis of Mesoporous NiO Nanoflake Array and Its Enhanced Electrochemical Performance for Supercapacitor Application, *J. Alloys Compd.*, 2014, **593**, p 184–189
35. D. Du, Z. Hu, Y. Liu, Y. Deng, and J. Liu, Preparation and Characterization of Flower-like Microspheres of Nano-NiO as Electrode Material for Supercapacitor, *J. Alloys Compd.*, 2014, **589**, p 82–87
36. J. Min, J. Liu, M. Lei, W. Wang, Y. Lu, L. Yang, Q. Yang, G. Liu, and N. Su, Self-Assembly of Parallelly Aligned NiO Hierarchical Nanostructures with Ultrathin Nanosheet Subunits for Electrochemical Supercapacitor Applications, *ACS Appl. Mater. Interfaces*, 2016, **8**, p 780–791
37. Y. Liu, C. Xiang, H. Chu, S. Qiu, J. McLeod, Z. She, F. Xu, L. Sun, and Y. Zou, Binary Co-Ni Oxide Nanoparticle-Loaded Hierarchical

- Graphitic Porous Carbon for High-Performance Supercapacitors, *J. Mater. Sci. Technol.*, 2020, **37**, p 135–142
38. J. Zhang, F. Liu, J.P. Cheng, and X.B. Zhang, Binary Nickel-Cobalt Oxides Electrode Materials for High-Performance Supercapacitors: Influence of Its Composition and Porous Nature, *ACS Appl. Mater. Interfaces*, 2015, **7**, p 17630–17640
 39. Q. Wang, Y. Zhu, J. Xue, X. Zhao, Z. Guo, and C. Wang, General Synthesis of Porous Mixed Metal Oxide Hollow Spheres with Enhanced Supercapacitive Properties, *ACS Appl. Mater. Interfaces*, 2016, **8**, p 17226–17232
 40. S.-H. Kazemi, B. Hosseinzadeh, H. Kazemi, M. Ali-Kiani, and S. Hajati, Facile Synthesis of Mixed Metal-Organic Frameworks: Electrode Materials for Supercapacitors with Excellent Areal Capacitance and Operational Stability, *ACS Appl. Mater. Interfaces*, 2018, **10**, p 23063–23073
 41. E.H. Liu, W. Li, J. Li, X.Y. Meng, R. Ding, and S.T. Tan, Preparation and Characterization of Nanostructured NiO/MnO₂ Composite Electrode for Electrochemical Supercapacitors, *Mater. Res. Bull.*, 2009, **44**, p 1122–1126
 42. X. Zheng, X. Yan, Y. Sun, Z. Bai, G. Zhang, Y. Shen, Q. Liang, and Y. Zhang, Au-Embedded ZnO/NiO Hybrid with Excellent Electrochemical Performance as Advanced Electrode Materials for Supercapacitor, *ACS Appl. Mater. Interfaces*, 2015, **7**, p 2480–2485
 43. J.J. Ruan, Y.Q. Huo, and B. Hu, Three-Dimensional Ni(OH)₂/Cu₂O/CuO Porous Cluster Grown on Nickel Foam for High Performance Supercapacitor, *Electrochim. Acta*, 2016, **215**, p 108–113
 44. A. Ray, A. Roy, P. Sadhukhan, S. Roy Chowdhury, P. Maji, S.K. Bhattacharya, and S. Das, Electrochemical properties of TiO₂-V₂O₅ nanocomposites as a high performance supercapacitors electrode material, *Appl. Surf. Sci.*, 2018, **443**, p 581–591
 45. D. Yao, Y. Ouyang, X. Jiao, H. Ye, W. Lei, X. Xia, L. Lu, and Q. Hao, Hierarchical NiO@NiCo₂O₄ Core-Shell Nanosheet Arrays on Ni Foam for High-Performance Electrochemical Supercapacitors, *Ind. Eng. Chem. Res.*, 2018, **57**, p 6246–6256
 46. R. Xu, J. Lin, J. Wu, M. Huang, L. Fan, Z. Xu, and Z. Song, A high-Performance Pseudocapacitive Electrode Material for Supercapacitors Based on the Unique NiMoO₄/NiO Nanoflowers, *Appl. Surf. Sci.*, 2019, **463**, p 721–731
 47. I. Chakraborty, N. Chakrabarty, A. Senapati, and A.K. Chakraborty, CuO@NiO/Polyaniline/MWCNT Nanocomposite as High-Performance Electrode for Supercapacitor, *J. Phys. Chem. C*, 2018, **122**, p 27180–27190
 48. W. Lei, P. He, Y. Wang, X. Zhang, A. Xia, and F. Dong, Solvothermal Preparation of Microspherical Shaped Cobalt-Manganese Oxide as Electrode Materials for Supercapacitors, *Compos. Sci. Technol.*, 2014, **102**, p 82–86
 49. K.R. Prasad and N. Miura, Electrochemically Synthesized MnO₂-Based Mixed Oxides for High Performance Redox Supercapacitors, *Electrochem. Commun.*, 2004, **6**, p 1004–1008
 50. A. Kirillova, C. Marschelke, and A. Synytska, Hybrid Janus Particles: Challenges and Opportunities for the Design of Active Functional Interfaces and Surfaces, *ACS Appl. Mater. Interfaces*, 2019, **11**, p 9643–9671
 51. S. Senobari and A. Nezamzadeh-Ejhi, A Comprehensive Study on the Enhanced Photocatalytic Activity of CuO-NiO Nanoparticles: Designing the Experiments, *J. Mol. Liq.*, 2018, **261**, p 208–217
 52. Y. Liu, L. Ma, D. Zhang, G. Han, and Y. Chang, A Simple Route to Prepare a Cu₂O-CuO-GN Nanohybrid for High-Performance Electrode Materials, *RSC Adv.*, 2017, **7**, p 12027–12032
 53. R. Jung, M. Metzger, D. Haering, S. Solchenbach, C. Marino, N. Tsiouvaras, C. Stinner, and H.A. Gasteiger, Consumption of Fluoroethylene Carbonate (FEC) on Si-C Composite Electrodes for Li-Ion Batteries, *J. Electrochem. Soc.*, 2016, **163**, p A1705–A1716
 54. M. Kuang, T.T. Li, H. Chen, S.M. Zhang, L.L. Zhang, and Y.X. Zhang, Hierarchical Cu₂O/CuO/Co₃O₄ Core-Shell Nanowires: Synthesis and Electrochemical Properties, *Nanotechnology*, 2015, **26**, p 304002

Publisher's Note Springer Nature remains neutral with regard to jurisdictional claims in published maps and institutional affiliations.